An IGBT Junction Temperature Estimation Method Based on Turn-Off Maximum di_C/dt With Decoupling Load Current

Yafei Shi, Boyang Zhang, Jianlong Kang, *Student Member, IEEE*, Yaokang Lai, Huai Wang, *Senior Member, IEEE*, and Zhen Xin, *Member, IEEE*

***Abstract*—Monitoring the junction temperature T_j of insulated gate bipolar transistor modules is crucial for reliable operation in medium/high voltage applications. Among the various temperature-sensitive electrical parameters, the maximum collector current falling rate di_C/dt_{max} is an effective indicator characterized by excellent linearity and amenability to real-time detection. However, current acquisition methods are prone to introduce parasitic parameters, and di_C/dt_{max} is also affected by the load current i_{load}. In response to these challenges, the printed circuit board Rogowski coil is proposed to measure di_C/dt_{max} and i_{load}, which can decouple the effect of i_{load}, and this method has the advantage of being contactless and integratable. In this article, the dependence of di_C/dt_{max} on T_j and i_{load} is theoretically analyzed. The system design of the Rogowski coil current sensor, including coil structure, integrator, and peak detection circuit is carried out. The effective bandwidth and measurement accuracy of the sensor are verified based on the vector network analyzer and the double pulse test, and the effectiveness of the method for T_j estimation is verified based on the buck converter.**

***Index Terms*—Insulated gate bipolar transistor (IGBT), integrator, junction temperature, maximum collector current falling rate (di_c/dt_{max}), printed circuit board (PCB) Rogowski coil.**

I. Introduction

POWER semiconductor devices are essential in power electronic conversion systems. They are one of the most reliability-sensitive electronic components and are particularly susceptible to thermal stress [1]. Junction temperature T_j monitoring of power devices could create additional value in terms of protection, operation optimization, and health monitoring [2]. Among various power devices, insulated gate bipolar transistor (IGBT) modules occupy an essential position in medium/high voltage applications [3], which means that T_j monitoring of IGBT is important to enhance reliability.

Typically, IGBT T_j monitoring methods can be categorized as physical contact-based, optical-based, thermal impedance-based, and temperature-sensitive electrical parameters (TSEPs)-based approaches [4]. Compared with other methods, the TSEPs methods are considered the most promising because of high accuracy, fast response, and nondestructive advantages [5]. The TSEPs methods can be classified into static and dynamic categories [6]. The on-state voltage with low current injection $v_{CEon(low)}$ is a commonly used static TSEP for IGBTs due to its simple design and no parameter dependents [7]. However, it requires a specific current source to inject a small current which is difficult to measure online. Another commonly used static TSEP is the on-state resistance R_{CEon}, which can be obtained online by measuring the v_{CEon} and collector current i_C. However, in addition to a current sensor, this method requires a clamping circuit to be designed and connected in parallel to the IGBTs to block high voltages during turn-OFF [8]. Evaluation of T_j by threshold voltage v_{th} is not affected by load current and bus voltage, but the v_{th} has low sensitivity and requires the connection of a voltage measurement circuit at the gate and an i_C sensor to determine the gate voltage at the reference current [9]. Turn-ON delay time t_{don} and turn-OFF delay time t_{doff} with good linearity can also be used as TSEPs, which are complicated by the need to connect high-bandwidth sensors and high-speed signal processing circuits [10], [11].

Bryant et al. [12] investigated and validated the maximum collector-emitter voltage change rate dv_{CE}/dt_{max} can be used as a TSEP to measure T_j. However, the measurement of dv_{CE}/dt_{max} requires a voltage measurement circuit in parallel on the IGBT and also requires complex differential calculations. A similar idea was proposed in [13], where the authors used the maximum collector current falling rate di_C/dt_{max} as a TSEP. The di_C/dt_{max} has good sensitivity and can be obtained by measuring the voltage drop of parasitic inductance between the power

Received 2 April 2024; revised 3 July 2024 and 31 July 2024; accepted 14 August 2024. Date of publication 26 August 2024; date of current version 12 December 2024. This work was supported by the National Natural Science Foundation of China under Grant 52377179, in part by the Hebei Provincial Department of Education Graduate Innovation Ability Training Funding Project CXZZBS2024035, and in part by the Hebei Provincial Department of Education Graduate Innovation Ability Training Funding Project CXZZSS2024015. An earlier version of this paper was presented at the IEEE Energy Conversion Congress and Exposition (ECCE), Detroit, USA, 9-13 October, 2022 [DOI: 10.1109/ECCE50734.2022.9947630]. Recommended for publication by Associate Editor Y. Zhang. *(Corresponding author: Zhen Xin.)*

Yafei Shi, Boyang Zhang, Jianlong Kang, and Zhen Xin are with the State Key Laboratory of EERI, Hebei University of Technology, Tianjin 300130, China (e-mail: 201821401030@stu.hebut.edu.cn; 202221401111@stu.hebut.edu.cn; 202011401012@stu.hebut.edu.cn; xzh@hebut.edu.cn).

Yaokang Lai is with the School of Electronic Engineering and Automation, Harbin Institute of Technology, Harbin 150006, China (e-mail: keytonell@163.com).

Huai Wang is with the Department of Energy, Aalborg University, 9220 Aalborg, Denmark (e-mail: hwa@energy.aau.dk).

Color versions of one or more figures in this article are available at https://doi.org/10.1109/TPEL.2024.3449551.

Digital Object Identifier 10.1109/TPEL.2024.3449551

TABLE I
SUMMARY OF THE CHARACTERISTICS OF DIFFERENT TSEPS AND PARAMETER SENSING METHODS

TSEP	Sensitivity	Dependent	Online	TSEP sensing method characteristic			
				Bandwidth	Invasive	Complexity	Ref
$v_{CEon(low)}$	Medium	T_j	No	Low	Yes	Low	[7]
R_{CEon}	Medium	T_j	Yes	Low	Yes	High	[8]
v_{th}	Low	T_j	Yes	High	Yes	High	[9]
t_{don}	Low	T_j	Yes	High	Yes	High	[10]
t_{doff}	Medium	T_j, i_C	Yes	High	Yes	High	[11]
dv_{CE}/dt_{max}	High	T_j, i_C, v_{DC}	Yes	High	Yes	High	[12]
di_C/dt_{max}	High	T_j, i_C, v_{DC}	Yes	High	Yes (Kelvin inductance)	Low	[13]
					No (Rogowski coil)	Low	[14]

and the Kelvin emitter of IGBT, which is characterized by its simplicity and cost-effectiveness. Nonetheless, it relies on the Kelvin structure and needs to be connected to the IGBT, which may introduce additional parasitic parameters. The Rogowski coil is an effective method for measuring di_C/dt_{max}, which is a magnetic sensing technology that exploits the principle of magnetic coupling to directly obtain the time derivative of the primary current [14]. The characteristics of the above-mentioned TSEPs are summarized in Table I.

From the table, it can be seen that most of the several commonly used measurement methods for TSEPs require contact with the power circuit, which is invasive. As the power and switching frequency of the power device increase, the voltage and current change rate will become larger, which means that parasitic parameters introduced by external measurement circuits may trigger high voltage overshoots and current overshoots [15]. Therefore, the di_C/dt_{max} is a promising TSEP because of its good sensitivity and the possibility of using the Rogowski coil for less invasive measurements. In previous research, the printed circuit board (PCB) Rogowski coils have been used to measure di/dt_{max} to evaluate the power device T_j [14], [16], but the effect of load current i_{load} is not considered, which makes it difficult to evaluate T_j in actual operating conditions where the i_{load} is uncertain.

To address the shortcoming, this article proposes to decouple i_{load} by modeling the dependence of di_C/dt_{max} on i_{load} and measuring i_{load} in real time by the PCB Rogowski coils. The decoupling of i_{load} removes its effect on the di_C/dt_{max}, thereby improving the accuracy of T_j estimation under varying current conditions. This enhancement enables di_C/dt_{max} to serve as an effective TSEP for IGBTs, improving its applicability across different operating conditions. Furthermore, the PCB Rogowski coils are used to online measure both di_C/dt_{max} and i_{load}. Compared to other measurement methods, PCB Rogowski coils offer the advantages of being noncontact and integratable, which makes the method particularly advantageous for applications sensitive to parasitic parameters and requiring compact spatial arrangements.

This article is organized as follows. Section II describes the turn-OFF characteristics of trench gate/field-stop IGBTs and analyses the dependence of the di_C/dt_{max} on T_j and i_{load}. Section III introduces the fundamental principle of the Rogowski coil and details the design of the coil and processing circuits including the integrator and peak detection circuit. Section IV verifies the coil effective bandwidth and the sensor measurement accuracy for di_C/dt, i_C, and di_C/dt_{max}. Section V demonstrates the linear relationship between peak detection circuit output voltage v_{speak} and both T_j and i_{load} under various operating conditions, and validates the effectiveness of the proposed method based on the buck converter. Section VI summarizes this article.

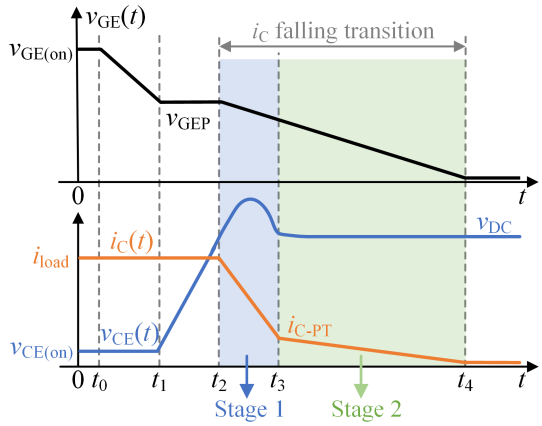

Fig. 1. Typical IGBT turn-OFF transient process.

II. DEPENDENCE OF DI_C/DT_{MAX} ON JUNCTION TEMPERATURE

A. Turn-Off Transient Analysis of IGBT

The typical IGBT turn-OFF process is shown in Fig. 1. Before the turn-OFF process starts, the voltage between the gate and emitter $v_{GE}(t)$ is the drive voltage $v_{GE(on)}$, the voltage between collector and emitter $v_{CE}(t)$ is the on-state voltage $v_{CE(on)}$, and the collector current $i_C(t)$ is load current i_{load}. Then, the $v_{GE}(t)$ drops from $v_{GE(on)}$ to the plateau voltage v_{GEP} (t_0–t_1), after which IGBT enters the Miller state, and the $v_{GE}(t)$ remains constant. During the Miller platform period (t_1–t_2), the $v_{CE}(t)$ rises from $v_{CE(on)}$, and when it reaches the busbar voltage v_{DC} means the end of the $v_{CE}(t)$ rise process. Meanwhile, $i_C(t)$ starts to drop from i_{load}, and the process can be divided into two stages. During stage 1 (t_2–t_3), $i_C(t)$ falls sharply from i_{load} to i_{C_PT} and an overshoot on $v_{CE}(t)$ appears due to varying collector current

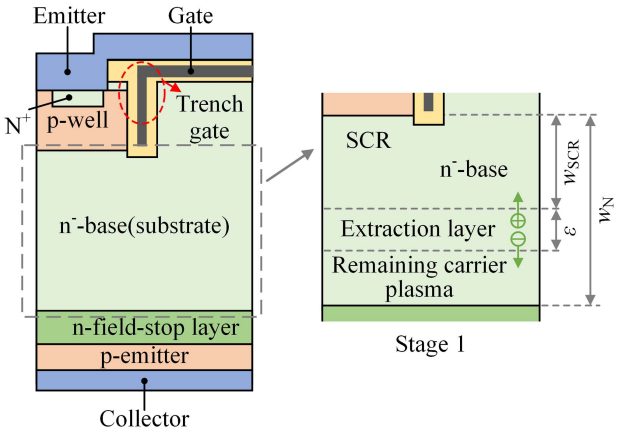

Fig. 2. Basic structure of the trench/field-stop IGBT and the structure of the n-base region during stage 1.

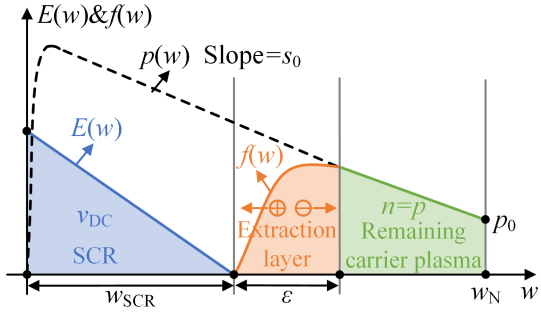

Fig. 3. Electric field and carrier concentration distribution in the n-base region.

through parasitic inductance. In this stage, the collector current falling properties are mainly governed by the storage carrier extraction behavior in the n-base region. At t_3, $i_C(t)$ starts to fall slowly from i_{C_PT} until zero (t_3–t_4). The recombination behavior of the carriers in this stage dominates the $i_C(t)$.

IGBT structures are constantly being improved as the demands of applications continue to increase. The trench gate/field-stop structure combines the trench cell and field-stop concepts, an advanced structure for high-power IGBTs, whose typical structure is shown in Fig. 2. Compared to planar IGBTs, the MOS channel of the trench gate device is vertical rather than horizontal when the IGBT is turned ON, which can eliminate the JFET effect, resulting in lower on-state impedance [17]. In addition, introducing the n-field-stop layer significantly reduces the thickness of the n-base region, which can improve turn-OFF speed and reduce losses.

Fig. 2 also illustrates the structure changes in the n-base region of the trench gate/field-stop IGBT during Stage 1 of current falling. The remaining excess holes in the n-base region are extracted to the emitter side, and the stored electrons are extracted to the collector side, which in turn forms the space charge region (SCR). In addition, there are two parts of the n-base region: one is the ongoing carrier extraction called the extraction layer, and the other is the remaining carrier plasma layer, which maintains the same carrier distribution as the on-state [18]. The widths of the SCR and the extraction layer are w_{SCR} and ε, respectively, and the width of the whole n-base region is w_N, which is shown in Fig. 2. The current falling characteristics of Stage 1 are mainly determined by the carrier behaviors in the extraction layer.

In Stage 2, the falling characteristics of $i_C(t)$ are mainly dominated by the carrier recombination mechanism. The transient time constant of the storage carrier recombination behavior is much larger than that of the extraction behavior [18]. Therefore, the maximum of the current change rate during IGBT turn-OFF occurs in Stage 1, and the falling characteristics of $i_C(t)$ in Stage 2 will not be described in detail in this article.

B. Storage Carrier Distribution Model

Fig. 3 illustrates the electric field and carrier concentration distribution in the n-base region during Stage 1. The curve of $E(w)$ implies the electric field in the n-base region. During the rise of $v_{CE}(t)$, the SCR expands in the region where the storage carriers are exhausted and establishes the electric field whose area enclosed with the w axis is v_{CE}. This area expands until v_{CE} equals v_{DC}.

The distribution curve of the carrier concentration during on-state is $p(w)$. The $p(w)$ is affected by the IGBT chip size, doping characteristics, and load current [19]. There are two critical parameters, the slope of the curve s_0 and the carrier concentration p_0 at $w = w_N$, as shown by the black dashed line in Fig. 3. Compared to the planar gate structure, trench gate IGBTs have $s_0 < 0$, which helps to balance the static and dynamic losses. s_0 is related to the collector current and carrier mobility, which can be expressed as

$$s_0 = -\frac{J_0\mu_p}{2qD_p\mu_n}\left[1-\gamma_{EON}-\gamma_{EON}\frac{\mu_n}{\mu_p}\right] \tag{1}$$

where q is the electronic charge (1.6×10^{-19}C), D_p is the hole diffusivity, J_0 is the steady-state collector current density, γ_{EON} is the hole injection efficiency at the P-collector and N-base junction, μ_n is the electron mobility, and μ_p is the hole mobility. p_0 depends on the carrier characteristics and the structure of the chip, and the expression is shown as follows [19]:

$$p_0 = \frac{J_0L_a\mu_p}{2qD_p\mu_n}\tanh\left(\frac{w_N}{L_a}\right)\left[1-\gamma_{EON}-\gamma_{EON}\frac{\mu_n}{\mu_p}\right] \tag{2}$$

where L_a is the ambipolar diffusion length.

During the current falling Stage 1, the characteristics of $i_C(t)$ are mainly determined by the extraction layer. As shown in the orange region in Fig. 3, the extraction layer can be specified by three parameters, namely, the carrier concentration distribution curve $f(w)$, the width of the extraction layer ε, and the start point location of the extraction layer w_{SCR}. The $f(w)$ can be described by a four-order polynomial in terms of the corresponding boundary conditions of the extraction layer, as follows [20]:

$$f(w) = s_0(w-w_{SCR}) + [p_0 - s_0(w_N - w_{SCR})]$$

$$\cdot\left[2\left(\frac{w-w_{\mathrm{SCR}}}{\varepsilon}\right)-2\left(\frac{w-w_{\mathrm{SCR}}}{\varepsilon}\right)^{3}+\left(\frac{w-w_{\mathrm{SCR}}}{\varepsilon}\right)^{4}\right]. \tag{3}$$

The ε can be calculated as [20]

$$\varepsilon(t)=\sqrt{{\varepsilon_0}^2+\frac{80}{3}\frac{b}{1+b}D_{\mathrm{p}}t} \tag{4}$$

where ε_0 is the initial extraction layer width of the current falling stage and $b=\mu_{\mathrm{n}}/\mu_{\mathrm{p}}$.

C. Dependence of the $-\mathrm{d}i_C/\mathrm{d}t_{max}$ on Junction Temperature Analysis

The MOS channel can be considered closed during the current falling stage, and the pure hole current maintains the total current at the emitter. According to the bipolar diffusion equation, the electron current density $J_{\mathrm{Cn}}(t)$ and the hole current density $J_{\mathrm{Cp}}(t)$ at the boundary between the SCR and the extraction layer ($w=w_{\mathrm{SCR}}$) are expressed as [13]

$$J_{\mathrm{Cn}}(t)=\frac{b}{1+b}J_{\mathrm{C}}(t)-qD_{\mathrm{a}}\left.\frac{\mathrm{d}f(w)}{\mathrm{d}w}\right|_{w_{\mathrm{SCR}}}=0 \tag{5}$$

$$J_{\mathrm{Cp}}(t)=\frac{1}{1+b}J_{\mathrm{C}}(t)+qD_{\mathrm{a}}\left.\frac{\mathrm{d}f(w)}{\mathrm{d}w}\right|_{w_{\mathrm{SCR}}}=J_{\mathrm{C}}(t) \tag{6}$$

where $J_{\mathrm{C}}(t)$ is the transient collector current density, and D_{a} is the ambipolar diffusivity. Differentiating $f(w)$ in (3) when $w=w_{\mathrm{SCR}}$, and bringing it into (5) and (6), $J_{\mathrm{C}}(t)$ can be given by

$$J_{\mathrm{C}}(t)=\frac{1+b}{b}qD_{\mathrm{a}}\left[s_0+\frac{2}{\varepsilon(t)}\left(p_0+s_0w_{\mathrm{SCR}}-s_0w_{\mathrm{N}}\right)\right]. \tag{7}$$

At the beginning of the current falling stage ($t=0$), ε_0 can be obtained from (7), as shown in (8). Taking the time derivative of (7), the maximum value of the collector current density falling rate $-\mathrm{d}J_{\mathrm{C}}(t)/\mathrm{d}t_{\max}$ is shown in (9)

$$\varepsilon_0=\frac{2qD_{\mathrm{a}}(1+b)(p_0+s_0w_{\mathrm{SCR}}-s_0w_{\mathrm{N}})}{bJ_0-s_0(1+b)qD_{\mathrm{a}}} \tag{8}$$

$$-\mathrm{d}J_{\mathrm{C}}(t)/\mathrm{d}t_{\max}=\frac{80}{3{\varepsilon_0}^3}qD_{\mathrm{a}}D_{\mathrm{p}}(p_0+s_0w_{\mathrm{SCR}}-s_0w_{\mathrm{N}}). \tag{9}$$

Using (1), (2) and (8) in (9) yields

$$-\mathrm{d}J_{\mathrm{C}}(t)/\mathrm{d}t_{\max}=\frac{40}{3}\frac{b}{(1+b)^3}\frac{{D_{\mathrm{p}}}^3}{{D_{\mathrm{a}}}^2}\frac{J_0}{\left(1-\gamma_{\mathrm{EON}}-\gamma_{\mathrm{EON}}\mu_{\mathrm{n}}/\mu_{\mathrm{p}}\right)^2}\cdot\frac{1}{\left[L_{\mathrm{a}}\tanh\left(w_{\mathrm{N}}/L_{\mathrm{a}}\right)+w_{\mathrm{N}}-w_{\mathrm{SCR}}\right]^2}. \tag{10}$$

The temperature-dependent factors in (10) are summarized in Table II [21]. Substituting the temperature-dependent expressions in Table II into (10), including μ_{n}, μ_{p}, D_{n}, D_{p}, and D_{a}, and performing simplification of the terms yields

$$-\mathrm{d}J_{\mathrm{C}}(t)/\mathrm{d}t_{\max}=3.95\times10^{9}\times\frac{k}{q}\frac{b}{(1+b)^3}\frac{1}{\left(1-\gamma_{\mathrm{EON}}-3.3\gamma_{\mathrm{EON}}\right)^2}\cdot\frac{J_0{T_{\mathrm{j}}}^{-1.5}}{\left[L_{\mathrm{a}}\tanh\left(w_{\mathrm{N}}/L_{\mathrm{a}}\right)+w_{\mathrm{N}}-w_{\mathrm{SCR}}\right]^2} \tag{11}$$

where q is 1.6×10^{-19} C, k is the Boltzmann constant (1.38×10^{-23} J/K), γ_{EON} usually has a value of 0.25 for large injections [19], and $b=\mu_{\mathrm{n}}/\mu_{\mathrm{p}}=3.3$. These parameters are usually constants and can be replaced by the constant c. The following equation is then obtained:

$$-\mathrm{d}J_{\mathrm{C}}(t)/\mathrm{d}t_{\max}=\frac{\mathrm{c}J_0{T_{\mathrm{j}}}^{-1.5}}{\left[L_{\mathrm{a}}\tanh\left(w_{\mathrm{N}}/L_{\mathrm{a}}\right)+w_{\mathrm{N}}-w_{\mathrm{SCR}}\right]^2}. \tag{12}$$

The normal operating junction temperature of IGBT power modules is between 298 K and 423 K [22]. Within this range, the ${T_{\mathrm{j}}}^{-1.5}$ can be approximated as $-6.2\times10^{-7}T_{\mathrm{j}}+3.74\times10^{-4}$. Therefore, the maximum value of the collector's current falling rate $-\mathrm{d}i_{\mathrm{C}}(t)/\mathrm{d}t_{\max}$ can be expressed as

$$-\mathrm{d}i_{\mathrm{C}}(t)/\mathrm{d}t_{\max}=\frac{i_{\mathrm{load}}(\mathrm{m}+\mathrm{n}T_{\mathrm{j}})}{\left[L_{\mathrm{a}}\tanh\left(w_{\mathrm{N}}/L_{\mathrm{a}}\right)+w_{\mathrm{N}}-w_{\mathrm{SCR}}\right]^2} \tag{13}$$

where i_{load} is the steady-state collector current and m, n are constant coefficients in the approximation equation. The expression for L_{a} is given in Table II, and it can be calculated to obtain that the L_{a} value of IGBT is constant and independent of temperature, with a value of about 40 μm [21]. w_{N} is related to the IGBT model and w_{SCR} is determined by the busbar voltage, and neither of these parameters is affected by temperature.

From (13), it can be seen that there is a linear relationship between $\mathrm{d}i_{\mathrm{C}}(t)/\mathrm{d}t_{\max}$ and T_{j}, while it is directly proportional to i_{load}. In addition, $\mathrm{d}i_{\mathrm{C}}(t)/\mathrm{d}t_{\max}$ is influenced by the bus voltage v_{DC}, as an increase in v_{DC} requires the expansion of SCR to withstand higher voltages, which leads to an increase in $-\mathrm{d}i_{\mathrm{C}}(t)/\mathrm{d}t_{\max}$. The excellent linearity of $\mathrm{d}i_{\mathrm{C}}(t)/\mathrm{d}t_{\max}$ with T_j allows it to be used as a TSEP, but the effects of load current and bus voltage should also be considered. Compared to the generally steady system bus voltage, the on-state current of IGBTs varies continuously throughout converter operation. Therefore, when monitoring the junction temperature of IGBTs in real-time, it is imperative to not only obtain the $\mathrm{d}i_{\mathrm{C}}(t)/\mathrm{d}t_{\max}$ but also to measure the i_{C} to effectively decouple the effect of i_{load} on the $\mathrm{d}i_{\mathrm{C}}(t)/\mathrm{d}t_{\max}$. In the next section, the design of the

TABLE II
TEMPERATURE-DEPENDENT FACTORS

Parameter	Symbol	Temperature-dependent expression
Electron mobility	μ_{n}	$\mu_{\mathrm{n}}(T_{\mathrm{j}})=1500(300/T_{\mathrm{j}})^{2.5}$
Hole mobility	μ_{p}	$\mu_{\mathrm{p}}(T_{\mathrm{j}})=450(300/T_{\mathrm{j}})^{2.5}$
Electron diffusivity	D_{n}	$D_{\mathrm{n}}(T_{\mathrm{j}})=\mu_{\mathrm{n}}(kT_{\mathrm{j}}/\mathrm{q})$
Hole diffusivity	D_{p}	$D_{\mathrm{p}}(T_{\mathrm{j}})=\mu_{\mathrm{p}}(kT_{\mathrm{j}}/\mathrm{q})$
Ambipolar diffusivity	D_{a}	$D_{\mathrm{a}}(T_{\mathrm{j}})=2D_{\mathrm{n}}D_{\mathrm{p}}/(D_{\mathrm{n}}+D_{\mathrm{p}})$
Ambipolar diffusion length	L_{a}	$L_{\mathrm{a}}(T_{\mathrm{j}})=(D_{\mathrm{a}}\tau_{\mathrm{HL}})^{0.5}$
High-level lifetime	τ_{HL}	$\tau_{\mathrm{HL}}(T_{\mathrm{j}})=\tau_{\mathrm{HL}}(300\mathrm{K})(T_{\mathrm{j}}/300)^{1.5}$

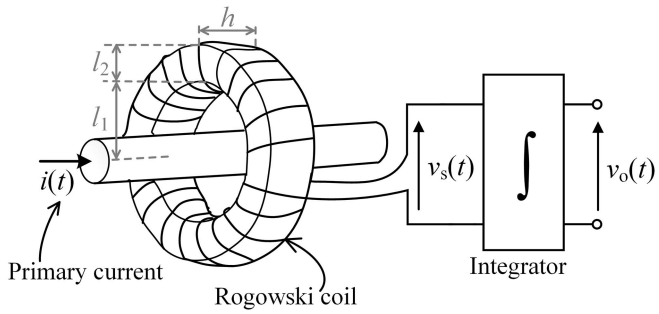

Fig. 4. Sketch of a Rogowski coil current sensor.

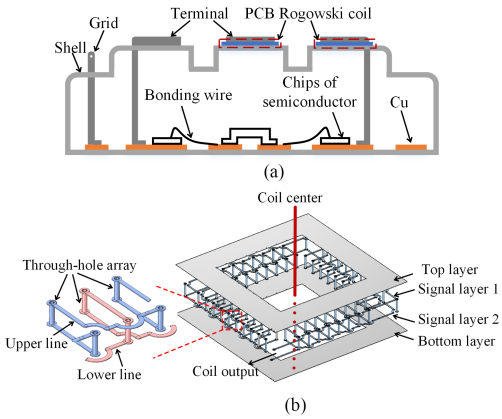

Fig. 5. PCB Rogowski coil (a) installation drawing in an IGBT power module. (b) Three-dimensional structure view.

Rogowski coil to enable the measurement of d$i_C(t)$/dt_{max} and i_C will be discussed.

III. Measuring Principle and Design of PCB Rogowski Coil

A. Operating Principle

The Rogowski coil is for measuring an alternating current using a winding on an air core. Its operating principles are based on Faraday's law and Ampere's circuital law [23]. To illustrate, Fig. 4 shows a simple schematic, where current $i(t)$ to be measured is in the primary conductor. An induced voltage, according to (14), can then be detected across the coil

$$v_s(t) = \frac{d\phi}{dt} = M\frac{di(t)}{dt} \tag{14}$$

where d$i(t)$/dt is the rate of primary current change, and M is the mutual inductance between the coil and primary conductor, which is determined by the dimensions and number of turns N of the coil winding, calculated as follows:

$$M = \frac{\mu_0 N h}{2\pi} \ln\frac{l_1 + l_2}{l_1} \tag{15}$$

where h is the width of the toroid, l_1 is the inside radius of the coil, and l_2 is the width of the winding. The implemented Rogowski coil needs to be connected to an integrator to recover the primary current. The coil and integrator, as the main components of a Rogowski coil current sensor, the design of which will be discussed in the following two sections.

B. Design of the Coil

Compared to other sensors, Rogowski coils can be designed in a rectangular shape PCB and nested on the power module terminals to improve space utilization, and the installation drawing is shown in Fig. 5(a). The design structure of the PCB Rogowski coil is shown in Fig. 5(b), which shows the four-layer PCB structure with the coil on the inner layers to receive signals and the shielding on the outer layers against electromagnetic interference. As for coil winding, it should not only be wound in one direction, but a return wire is needed to wound back to counteract the coupling of the vertical magnetic field [24], as shown in the enlarged view of the winding in Fig. 5(b).

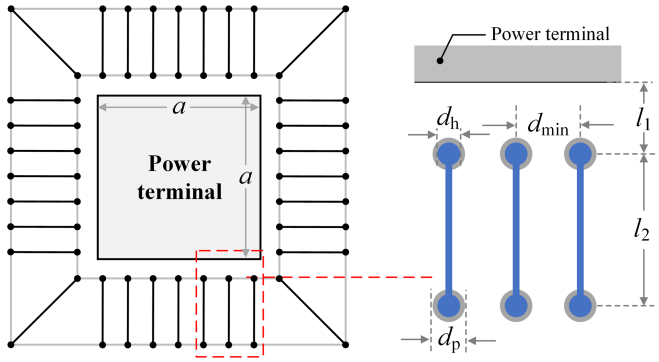

Fig. 6. Schematic diagram of the coil size.

The number of turns N is an important parameter because it determines the coil sensitivity, with more turns resulting in great sensitivity. However, it is limited by the size and spacing of the through-hole. The dimensions of the through-hole and winding in the coil are shown in Fig. 6. According to the standards in [25], the minimum through-hole diameter for multilayer PCB d_h is 0.2 mm, and the minimum pad size is determined by the following equation:

$$d_p = d_h + 2b + c \tag{16}$$

where d_h is the through-hole diameter, b is the minimum annular ring requirement, and c is the standard fabrication allowance. The minimum spacing between two through-holes d_{min} needs to be at least three times the pad width for ease of PCB installation [26]. Then, the maximum number of turns N_{max} can be obtained

$$N_{max} = 4\left(\frac{a}{d_{min}} + 1\right) \tag{17}$$

where a is the side length of the power terminal. The l_1 and l_2 are determined by the safe electrical spacing and the spacing between the terminals. Based on these, the various parameters of the designed coil size are shown in Table III.

In addition to sensitivity, the N also affects the bandwidth of the coil, with an increase turns leading to a decrease in bandwidth. The optimization of the N requires the determination

TABLE III
PARAMETERS OF THE PCB ROGOWSKI COIL SIZE

Parameter	Symbol	Value
Through-hole diameter	d_h	0.2 mm
Pad diameter	d_p	0.45 mm
Through-holes distance	d_{min}	0.8 mm
Inside length	l_1	1.5 mm
Winding width	l_2	3.2 mm
Terminal side length	a	12 mm
Wingding thickness	h_w	1.2 mm
PCB thickness	h_{pcb}	1.6 mm
Turns	N	64

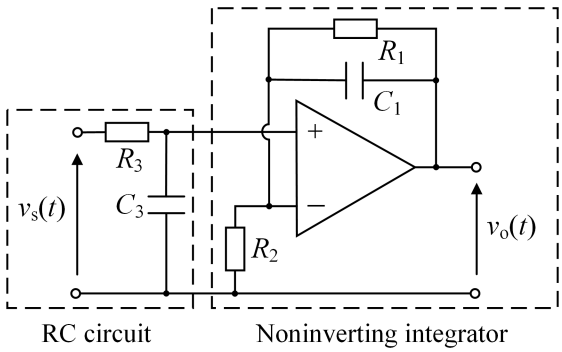

Fig. 7. Hybrid integrator with RC circuit and noninverting integrator.

of the maximum number of turns according to PCB design rules and installation space. The coil bandwidth with the maximum number of turns should be measured and compared to the sensor bandwidth required for the actual waveform being measured. If the coil bandwidth is not sufficient, the N needs to be reduced until the measurement requirements are met. The advantage of this optimization method is that it ensures as high a sensitivity as possible while satisfying the measurement bandwidth, thus achieving a higher signal-to-noise ratio. The measurement results of the coil bandwidth in this study are presented in Section IV-A.

C. Design of the Integrator

As described in Section III-A, the coil output voltage is proportional to the time derivative of the measured current, and an additional integration circuit is required to recover the measured current. Compared to passive integration circuits, the active integrator consists of analog operational amplifiers (OPAs), which are not susceptible to variations of component values and termination at its output. The included amplifier can either be of the inverting or noninverting type. The noninverting integrator avoids the negative effects of ringing and preshoot, which is considered to be an optimal integrator topology [27]. To extend the bandwidth, the noninverting integrator needs to be coupled with an RC circuit to form a hybrid integrator. The topology of the hybrid integrator is shown in Fig. 7. Between the negative terminal and the output of the OPA, an integrating capacitor C_1

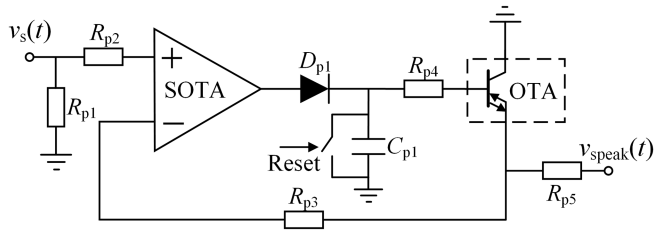

Fig. 8. Schematic of the peak detection circuit.

and a large resistor R_1 are usually connected in parallel. The function of R_1 is to limit the low-frequency gain, which if not constrained, will excessively amplify the low-frequency noise and saturate the integrator. The transfer function is expressed as

$$H(s) = \frac{1}{R_3C_3s+1}\cdot\frac{R_1R_2C_1s+R_1+R_2}{R_1R_2C_1s+R_2} = \frac{R_1R_2C_1s+R_1+R_2}{R_1R_2R_3C_1C_3s^2+(R_1R_2C_1+R_2R_3C_3)s+R_2}. \tag{18}$$

There is an essential requirement for the passive component value of the hybrid integrator

$$f_c = \frac{1}{2\pi R_2C_1} = \frac{1}{2\pi R_3C_3}. \tag{19}$$

This means that below the cut-OFF frequency f_c, the integration is done by the noninverting integrator, while above-mentioned f_c, it is done by the RC circuit. Therefore, as long as (19) is satisfied, the infinite extension of the high-frequency integration and smooth integration transitions at f_c can be realized. To prevent large bias voltages from entering the OPA, the values of R_2 and R_3 should not be too large, and they are set to 80 Ω in this work. According to (19), the f_c is determined as 100 kHz, and C_1 and C_3 are set to 20 nF. R_1 is set to 250 kΩ to reduce the transfer gain at low frequencies. An OPA THS4631 with a gain bandwidth of 300 MHz is selected as the noninverting integrator OPA.

D. Design of the Peak Detection Circuit

In this article, the OPA615 chip is used to achieve peak detection, and the schematic is shown in Fig. 8. The OPA615 consists of an operational transconductance amplifier (OTA) and a fast and accurate sampling OTA with bandwidths of 710 and 730 MHz, respectively [28]. C_{p1} is the holding capacitor for energy storage and D_{p1} is the diode to ensure unidirectional signal flow. The OPA615 as a current mode amplifier has better ac performance than a voltage mode amplifier. This is because charging a capacitor at a constant voltage results in a slower charging rate over time, whereas the capacitor voltage increases linearly at a constant current [29].

The value of C_{p1} affects the available bandwidth as well as the circuit stability. The larger the value, the more stable the circuit is but the lower the bandwidth. When C_{p1} is selected as 47 pF, the effective bandwidth is 48 MHz, which is sufficient for the measurement requirements [28]. A reset switch is connected in

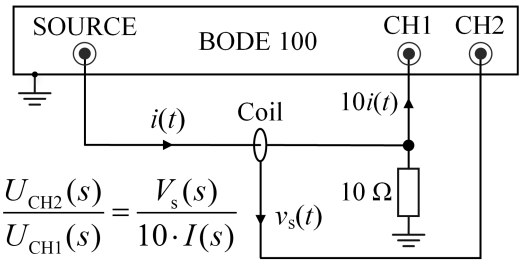

Fig. 9. Measurement configurations for the Rogowski coil frequency characteristics.

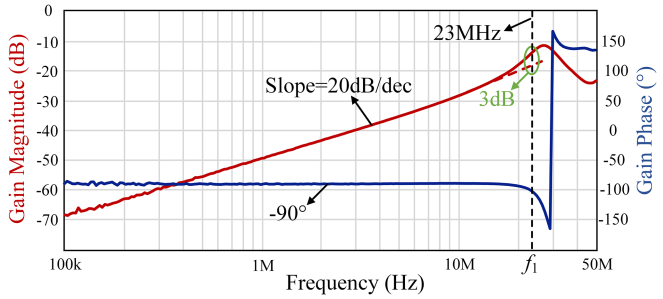

Fig. 10. Measurement results of the Rogowski coil frequency characteristics.

parallel at C_{p1} for discharging. R_{p1} and R_{p5} are input and output resistors used for impedance matching with the value of 50 Ω. R_{p2} and R_{p4} serve for de-Q-ing of the trace and package parasitic LC while eliminating output offset voltage due to input bias currents, which take the values of 150 and 100 Ω, respectively [29]. R_{p3} is in the voltage feedback loop, which takes the value of 300 Ω. Note that the input signal to the circuit should be positive, so when the coil outputs a negative voltage it is necessary to access an inverter or change the winding direction.

Typically the output voltage of the peak detection circuit will droop after reaching the maximum value, making an error between the final hold value and peak value. The droop effect of the peak detection circuit is mainly caused by the discharge of the C_{p1}. There are several main factors causing the droop: OPAs input bias current, diode reverse recovery current, and capacitor leakage current. To reduce the droop effect, the OPA615 chip with a very low bias current (1 μA) is suitable. The diode is required to have a small reverse recovery current, and the Schottky diode 1N60 is chosen in this study. Holding capacitors need to be selected with the lowest possible leakage current. The peak detection circuit proposed in this article significantly reduces the droop error and can guide the circuit design. The measurement results are shown in Section IV-B.

IV. Prototype Implementation and Coil Measurement Accuracy Verifications

A. Rogowski Coil Transfer Characteristics Measurement

The frequency response of the Rogowski coil can reflect the sensitivity and effective bandwidth of the sensor. In this section, the vector network analyzer (BODE 100) is used to test the transfer characteristics of the coil [30]. The schematic diagram for testing the Rogowski coil transfer characteristics is shown in Fig. 9. The signal is emitted from the SOURCE and transmitted through a 10-Ω resistor to simulate the measured current $i(t)$. The coil is nested in the line to measure $i(t)$. The CH1 receives the sampled voltage of 10 times $i(t)$, and the CH2 receives the induced voltage $v_s(t)$ from the coil. The ratio of the induced voltage to the sampled signal (CH2/CH1) gives the frequency response of the coil. It should be noted that the amplitude of the frequency characteristic curve obtained by this configuration is one-tenth of the coil's true transfer characteristic.

The frequency response curve is shown in Fig. 10. The effective frequency of the sensor is usually defined at the 3 dB bandwidth point [30]. It can be seen that the cut-OFF frequency of the coil is 23 MHz, which is determined by the parasitic parameters of the coil. When the measuring frequency f_{meas} is less than 23 MHz ($f_{meas} < f_1$), the output voltage of the coil has a differential relationship with the measured current (slope = 20 dB/dec, phase = 90°).

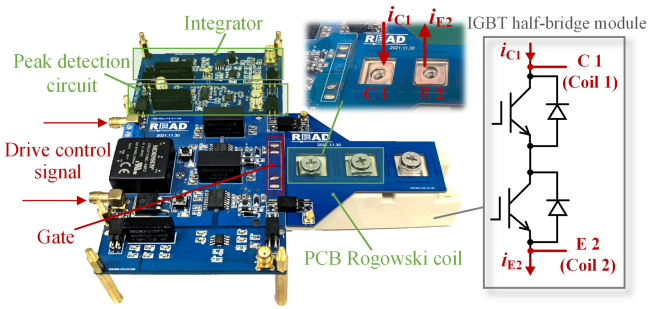

Fig. 11. Prototype of PCB Rogowski coil integrated with gate driver circuit.

In this study, the gate resistance of the IGBT is set to 5 Ω, in which case its fall time t_f is usually around 100 ns. According to the formula (BW = 0.35/t_f), the sensor required bandwidth BW can be calculated to be 3.5 MHz, of which three to five times BW is usually chosen as the final bandwidth to ensure measurement accuracy [31]. Therefore, the bandwidth of 23 MHz is sufficient for the turn-OFF current measurement of the used IGBTs and $N = 64$ can be used as the optimal choice of the number of turns of coil.

B. di_C/dt, i_C, and di_C/dt_{max} Sensing Experiments

A prototype of PCB Rogowski coil nested on the terminals of the IGBT power module (Infineon FF75R12RT4) and integrated with the gate driver circuit is demonstrated in Fig. 11. The coils can be wound around the upper collector C1 and lower emitter E2 of the half-bridge module to measure the current flowing through the upper and lower IGBTs. The processing circuits including the integrator and peak detection circuit are connected to the coil through the connector. The coils output the voltage signal v_s to characterize di_C/dt, the peak detection circuit outputs the voltage v_{speak} to characterize di_C/dt_{max}, and the integrator output the voltage v_o to characterize i_C.

The double pulse test platform is built to verify the measurement accuracy of the Rogowski coil sensor, and the lower IGBT

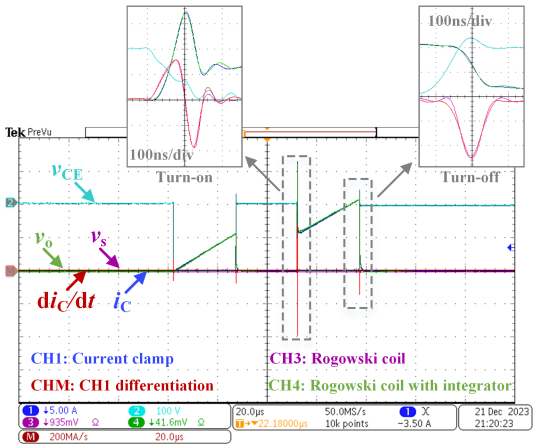

Fig. 12. i_C and di_C/dt measurement results based on the double-pulse test.

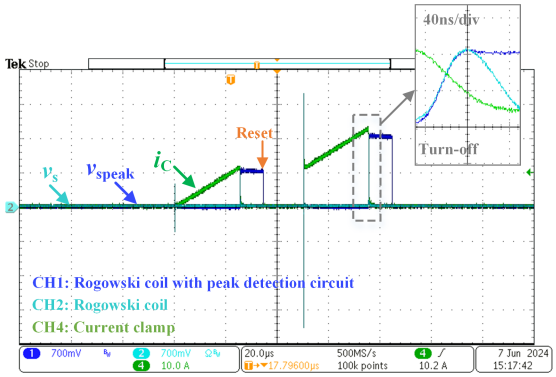

Fig. 13. di_C/dt_{max} measurement results based on the double-pulse test.

is used as the device under test. When the driving resistance is 5 Ω, the switching frequency is 20 kHz, and the duty cycle is 50%, the measurement results are shown in Fig. 12. The blue waveform (CH1) is the i_C measured by a current clamp (Tektronix TCP 0030A), the red waveform (CHM) is the di_C/dt, which is obtained by differentiating CH1 with the oscilloscope, the pink waveform is the coil output voltage v_s, and the green waveform is the integrator output voltage v_o. According to the detailed magnified figure, the waveforms of CHM and CH3 almost overlap at the turn-ON and turn-OFF moments. The sensitivity is 4700 mV/A·ns, which corresponds to the frequency response curve in Fig. 10, which means that the peak coil output voltage can accurately characterize the $di_C(t)/dt_{max}$. Comparing the waveforms of CH1 and CH4, the Rogowski coil can accurately measure i_C both during on-state and switching moments, and the sensitivity is 8.3 mV/A. Based on the above-mentioned experiments, the PCB Rogowski coil can not only accurately measure the IGBT di_C/dt, but also accurately restore the i_C by connecting an integrator.

The measurement results of the peak detection circuit based on the double pulse test are shown in Fig. 13. The CH4 waveform is the i_C measured by a current clamp, the CH2 waveform is the coil output voltage v_s, and the CH1 waveform is the peak detection circuit output voltage v_{speak}. As can be seen from the zoomed-in

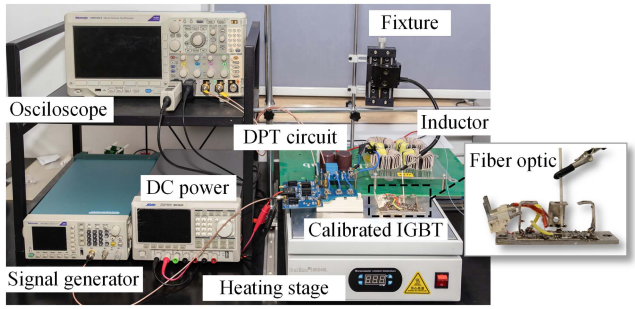

Fig. 14. Junction temperature measurement platform based on double-pulse test.

detail, the peak detection circuit output voltage can follow the coil output voltage well and hold at the peak value to accurately obtain di_C/dt_{max}. The reset signal is triggered sometime after the end of the turn-OFF process to extract the di_C/dt_{max} for each cycle.

V. Dependence and Junction Temperature Estimation Results

A. Dependence of v_{speak} on T_j

In order to verify the linear relationship between IGBT $di_C(t)/dt_{max}$ and T_j, the double pulse test platform with variable T_j is shown in Fig. 14, where the Rogowski coil current sensor is used to measure the $di_C(t)/dt_{max}$ and $i_C(t)$. The IGBT module under test is heated using a heating stage. An additional calibrated IGBT module is placed on the heating stage in a position symmetrical to the IGBT under test, and the molded case of the calibrated IGBT module is removed to expose the chip. A fiber optic probe (Opsens Solutions OTG-F) is used to obtain the actual T_j by contacting the calibrated IGBT chip, and a fixture is used to hold the probe in place. This solution calibrates the error between the heating stage setup temperature and the actual junction temperature.

The double pulse test is performed at six junction temperatures of 25, 50, 75, 100, 125, and 150 °C, respectively. With $v_{DC} = 400$ V and $i_{load} = 40$ A, the collector current waveforms and the current change rate waveforms measured by the Rogowski coil at the turn-OFF moment are shown in Fig. 15. From Fig. 15(a), it can be seen that the turn-OFF collector current will enter the trailing current phase earlier as the T_j increases, which makes the current change rate slower. This is because the increase in T_j will result in more remaining carriers in the n^--base region. Fig. 15(b) more clearly shows the variation rule of the turn-OFF collector current change rate with T_j. It can be seen that the amplitude of $di_C(t)/dt_{max}$ will decrease as the T_j increases.

B. Dependence of v_{speak} on i_{load}

According to (13), it can be seen that di_C/dt_{max} has a positive proportional relationship with i_{load}. To verify this conclusion, the double pulse test is carried out at different T_j and i_{load} with $v_{DC} = 400$ V. The relationship curves obtained by extracting

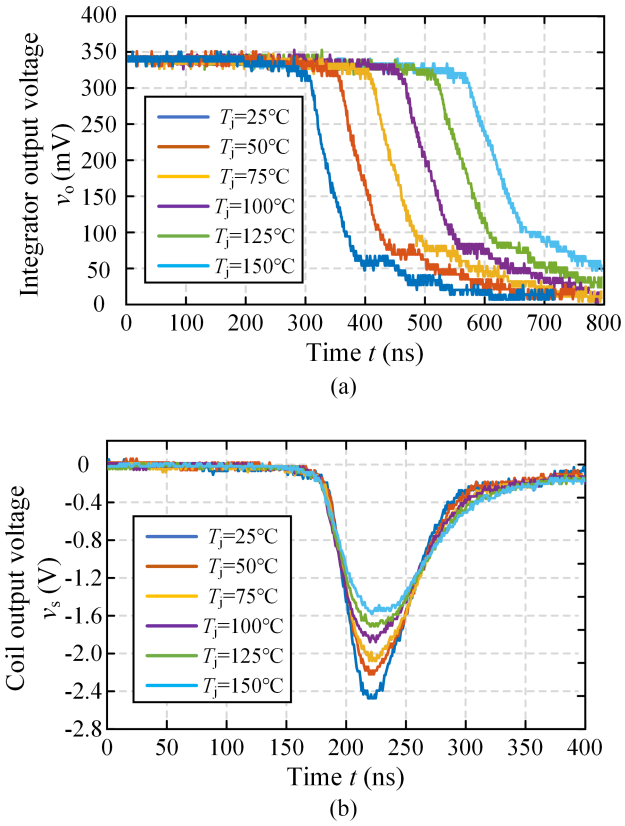

Fig. 15. Turn-OFF collector currents and change rates measured by Rogowski coil at different T_j. (a) Integrator output voltage. (b) Coil output voltage.

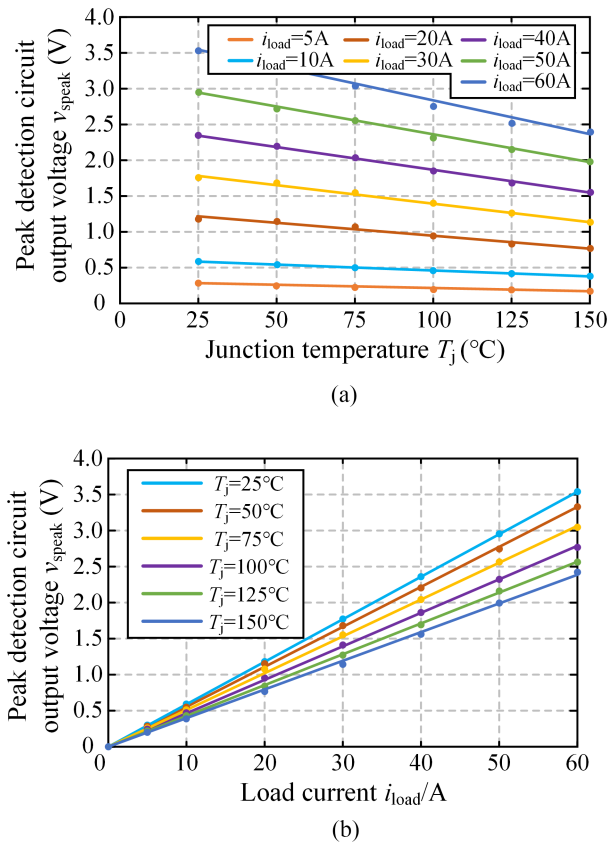

Fig. 16. Peak detection circuit output voltage with (a) different T_j and (b) different i_{load}.

the v_{speak} values are shown in Fig. 16. Fig. 16(a) illustrates the trend of v_{speak} as a function of T_j under different i_{load}, where i_{load} assumes values of 5, 10, 20, 30, 40, 50, and 60 A. Across all i_{load} levels, a clear linear correlation is observed between v_{speak} and T_j. Fig. 16(b) shows the curve between v_{speak} and i_{load} for several T_j, where six T_j of 25, 50, 75, 100, 125, and 150 °C are selected. It can be seen that v_{speak} and i_{load} show a positive relationship regardless of T_j, which corresponds to (13). This means that the effect of i_{load} can be decoupled when using di_C/dt_{max} to reflect T_j.

To verify the effectiveness of i_{load} decoupling, the multipulse test is used to simulate continuously varying i_{load}. In the multipulse experiments, the v_{speak} (characterize di_C/dt_{max}) and v_o (characterize i_{load}) of the IGBT turn-OFF moment are obtained several times. The estimated junction temperature T_{jest} is calculated based on the calibration curve and compared with the actual temperature T_{jact} measured by the optical fiber to verify the accuracy of the T_j estimation under different i_{load}. The multipulse with eight pulses, v_{DC} = 400 V, a switching frequency of 50 kHz, and a duty cycle of 50% is tested as a case. According to the results in Fig. 16(a), the junction temperature calibration curve at v_{DC} = 400 V is as follows:

$$T_j = 386.5 - \frac{v_{speak}}{0.02 v_o}. \tag{20}$$

TABLE IV
T_j ESTIMATION RESULTS BASED ON MULTIPULSE TEST

Pulse	i_{load} (A)	v_o (mV)	T_{jact} = 25 °C			T_{jact} = 125 °C		
			v_{speak} (mV)	T_{jest} (°C)	ΔT_j (°C)	v_{speak} (mV)	T_{jest} (°C)	ΔT_j (°C)
1	4.1	33.1	237	28.5	3.5	172	126.7	1.7
2	8.1	66.2	476	27	2	348	123.7	1.3
3	12.2	100.3	720	27.6	2.6	517	128.8	3.8
4	16.3	134.3	978	23.4	1.6	707	123.4	1.6
5	20.3	168.0	1219	23.7	1.3	876	125.8	0.8
6	24.4	201.8	1443	28.4	3.4	1038	128.9	3.9
7	28.4	234.6	1689	24.6	0.4	1226	125.2	0.2
8	32.5	271.0	1947	27.3	2.3	1405	127.6	2.6

The multipulse tests are performed at two junction temperatures, T_j = 25 °C and T_j = 125 °C, and the T_{jest} obtained based on (20) are shown in Table IV.

From the table, it can be seen that T_{jest} can be obtained from the same calibration curve at different i_{load} with an error of less than 4 °C. This means that the calibration curve equation can be applied to various i_{load}, thus verifying the effectiveness of the proposed load current decoupling method.

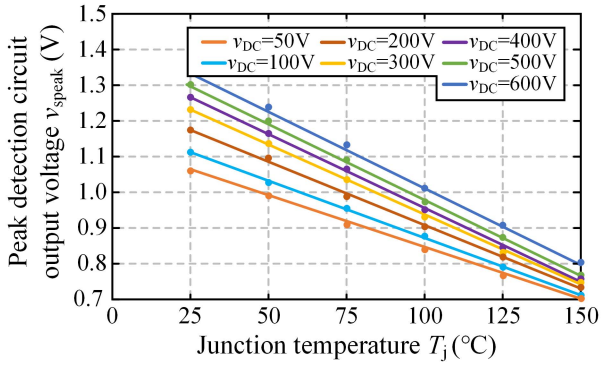

Fig. 17. Peak detection circuit output voltage with different T_j at different v_{DC}.

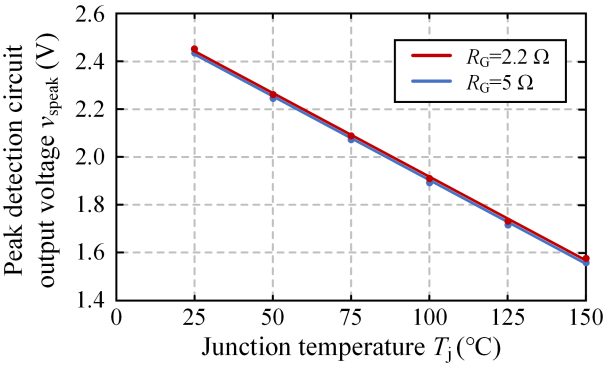

Fig. 18. Peak detection circuit output voltage with different T_j at different R_G.

C. Dependence of v_{speak} on v_{DC}

In Section II-C, it is analyzed that v_{DC} affects di_C/dt_{max} because an increase in v_{DC} requires the SCR to expand, which leads to an increase in di_C/dt_{max}. The linear relationship between v_{speak} and T_j at $i_{load} = 20$ A persists under different v_{DC}, as demonstrated in Fig. 17, where v_{DC} assumes values of 50, 100, 200, 300, 400, 500, and 600 V.

Although the direct function of v_{DC} and di_C/dt_{max} is not obtained, it can still be applied in actual converters by calibrating in advance. For example, in a single-phase full-bridge inverter with $v_{DC} = 400$ V, the v_{speak} with different T_j for $v_{DC} = 400$ V can be measured in advance by the double pulse test with a heating stage to obtain the calibration curve. Then the single-phase full-bridge inverter IGBT T_j can be estimated in real time by obtaining v_{speak} and v_o and bringing them into the precalibrated curve.

D. Dependence of v_{speak} on R_G

In order to verify the linearity of di_C/dt_{max} with T_j for smaller driving resistance R_G, the double pulse test is performed at $R_G = 2.2\ \Omega$, where v_{DC} and i_{load} are set to 400 V and 40 A, respectively. The measured v_{speak} is shown in Fig. 18 at T_j of 25, 50, 75, 100, 125, and 150 °C, respectively. It can be seen that the v_{speak} has a good linear relationship with T_j at $R_G = 2.2\ \Omega$, and the v_{speak} of each T_j node at $R_G = 2.2\ \Omega$ is close to the value at $R_G = 5\ \Omega$. This is due to the fact that the internal R_G of this IGBT is 10 Ω [32], so the external R_G has a weak effect on the di_C/dt_{max} when the external driving resistance is small.

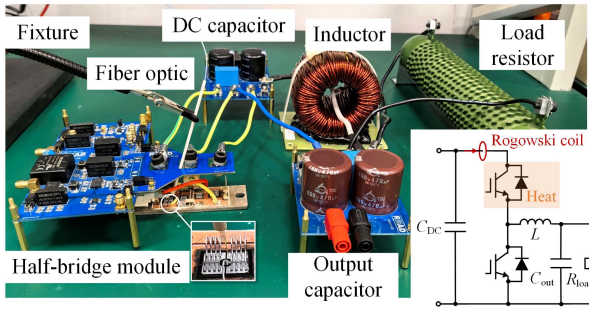

Fig. 19. Schematic and platform of the buck converter.

E. T_j Estimation Results

To verify the accuracy of the method, v_{speak} and v_o are obtained based on three conditions of 200 V 20 A, 400 V, 40 A, and 600 V 60 A, respectively, and the calculated value of T_j is obtained based on the calibration curve. According to the results in Fig. 17, the junction temperature calibration curves at v_{DC} of 200 V and 600 V are as follows:

$$T_j = 388.2 - \frac{v_{speak}}{0.0192 v_o} \tag{21}$$

$$T_j = 383.6 - \frac{v_{speak}}{0.022 v_o}. \tag{22}$$

When the temperature of the heating stage is set from 20 to 180 °C with a step of 20 °C, the actual junction temperature T_{jact} measured by the fiber optic probe and the estimated junction temperature T_{jest} are shown in Table V. From the table, the error ΔT_j between T_{jest} and T_{jact} is less than 4 °C.

To validate the effectiveness of the proposed method in a real converter, T_j is estimated for the IGBT in the dc–dc buck converter. The schematic and the platform of the buck converter are shown in Fig. 19. The buck operation mode can be realized based on an IGBT half-bridge module. The upper device heats up during circuit operation and is used as the device under test. The module is opened and a fiber optic probe is used to measure the T_j of the upper IGBT in actual operation. The upper IGBT di_C/dt and i_C are measured by nesting a Rogowski coil on the module collector terminals. The buck converter has a bus capacitor C_{DC} of 220 μF, an output capacitor C_{out} of 235 μF, an inductor L of 1 mH, and a load resistor R_{load} of 4 Ω.

When the bus voltage is 200 V, the switching frequency is 20 kHz, and the duty cycle is 35%, the measurement results are shown in Fig. 20. The CH1 waveform is the v_{CE} measured by a passive probe, the CH2 waveform is the coil output voltage v_s, the CH3 waveform is the peak detection circuit output voltage v_{speak}, and the CH4 waveform is the integrator output voltage v_o. From the turn-OFF waveform detail, it can be seen that the v_{speak} can follow the v_o well and hold at the peak value to accurately obtain di/dt_{max}. At this moment, the values of v_{speak} and v_o are 642 and 142 mV, respectively, and the junction temperature

TABLE V
JUNCTION TEMPERATURE ESTIMATION RESULTS AT v_{DC} = 200 V, v_{DC} = 400 V, AND v_{DC} = 600 V

v_{DC} = 200 V i_{load} = 20 A					v_{DC} = 400 V i_{load} = 40 A					v_{DC} = 600 V i_{load} = 60 A				
v_o (mV)	v_{speak} (mV)	T_{jest} (°C)	T_{jact} (°C)	ΔT_j (°C)	v_o (mV)	v_{speak} (mV)	T_{jest} (°C)	T_{jact} (°C)	ΔT_j (°C)	v_o (mV)	v_{speak} (mV)	T_{jest} (°C)	T_{jact} (°C)	ΔT_j (°C)
169	1201	18.1	18.8	0.7	332	2444	18.4	18.8	0.4	496	4015	15.7	18.8	3.1
169	1140	36.9	37.6	0.7	336	2340	38.3	37.6	0.7	492	3760	36.2	37.6	1.4
167	1075	52.8	56.4	3.6	332	2200	55.2	56.4	1.2	494	3545	57.4	56.4	1.0
169	1020	73.9	75.2	1.3	332	2080	73.3	75.2	1.9	496	3340	77.5	75.2	2.3
167	950	91.5	94.1	2.6	332	1930	95.8	94.1	1.7	492	3100	97.2	94.1	3.1
167	890	110.6	112.8	2.2	334	1810	115.5	112.8	2.7	492	2900	115.7	112.8	2.9
165	820	129.4	131.6	2.2	332	1670	135	131.6	3.4	490	2680	135	131.6	3.4
165	760	148.3	150.4	2.1	330	1540	153.3	150.4	2.9	490	2480	153.5	150.4	3.1
165	700	167.2	169.2	2	332	1440	169.7	169.2	0.5	494	2320	170.1	169.2	0.9

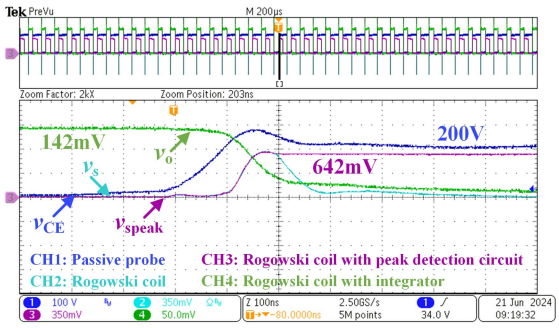

Fig. 20. i_C and di_C/dt_{max} measurement results based on the buck converter.

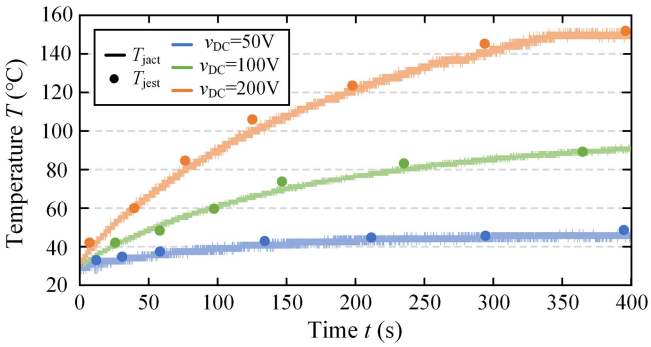

Fig. 21. T_j estimation results based on buck converter at different v_{DC}.

measured using the fiber optic probe is 150 °C. Substituting v_{speak} = 642 mV and v_o = 142 mV into (21) yields the calculated junction temperature T_{jest} of 152.7 °C, which has an error of 2.7 °C.

Further, the buck converter is operated at different operating conditions with v_{DC} of 50, 100, and 200 V. The T_{jact} rise curve of the IGBT from the start of operation to temperature stabilization is detected using a fiber optic probe and the results are shown in Fig. 21. The v_o and v_{speak} are also recorded several times throughout the heating process and the estimated junction temperature T_{jest} is calculated according to the calibration equations, where the calibration equations for 50 and 100 V can be obtained according to the curves of Fig. 17. The results of the T_{jest} are also shown in Fig. 21. It can be seen that the T_{jest} points are in the vicinity of the T_{jact} when the buck converter is operated at different conditions, which verifies the validity of the proposed method in actual operating conditions.

VI. CONCLUSION

A novel junction temperature estimation and load current decoupling method for trench gate/field-stop IGBTs based on turn-OFF d$i_C(t)$/dt_{max} is proposed in this article. The PCB Rogowski coil is proposed to measure d$i_C(t)$/dt_{max} and i_{load}, which can be nested at the power module terminals and integrated with the gate drive circuit. Compared with the existing T_j measurement solutions, this article decouples the effect of i_{load} to make d$i_C(t)$/dt_{max} a valid TSEP for IGBTs operating at different i_{load}, and this article enables online di_C/dt_{max} and i_{load} measurement using only the PCB Rogowski coil, which offers the advantage of being contactless and integratable.

In this article, the dependence model of di_C/dt_{max} on T_j and i_{load} is established based on the IGBT carrier characteristics. The coils are designed with maximum turns and differential windings to ensure maximum sensitivity and immunity against electromagnetic interference. Moreover, the noninverting integrator and peak detection circuit are designed to achieve i_{load} and peak of di_C/dt precise measurement. The frequency response of the coil is measured by a vector network analyzer, which shows the effective bandwidth is 23 MHz. The measurement accuracy of di_C/dt, i_C, and di_C/dt_{max} is verified based on a double pulse test, and the linear relationship between v_{speak} and T_j is also verified by the double pulse test at different i_{load}, v_{DC}, and R_G. The effectiveness of the proposed method is verified under actual operating conditions based on the dc–dc buck converter.

REFERENCES

[1] U.-M. Choi, F. Blaabjerg, and K.-B. Lee, "Study and handling methods of power IGBT module failures in power electronic converter systems," *IEEE Trans. Power Electron.*, vol. 30, no. 5, pp. 2517–2533, May 2015.

[2] H. Wang, M. Liserre, and F. Blaabjerg, "Toward reliable power electronics: Challenges, design tools, and opportunities," *IEEE Ind. Electron. Mag.*, vol. 7, no. 2, pp. 17–26, Jun. 2013.
[3] A. Arya, A. Chanekar, P. Deshmukh, A. Verma, and S. Anand, "Accurate online junction temperature estimation of IGBT using inflection point based updated I-V characteristics," *IEEE Trans. Power Electron.*, vol. 36, no. 9, pp. 9826–9836, Sep. 2021.
[4] Y. Yang, Q. Zhang, and P. Zhang, "A fast IGBT junction temperature estimation approach based on on-state voltage drop," *IEEE Trans. Ind. Appl.*, vol. 57, no. 1, pp. 685–693, Jan./Feb. 2021.
[5] X. Jiang et al., "Online junction temperature measurement for SiC MOSFET based on dynamic threshold voltage extraction," *IEEE Trans. Power Electron.*, vol. 36, no. 4, pp. 3757–3768, Apr. 2021.
[6] Y. Chen et al., "A thermo-sensitive electrical parameter with maximum dIC/dt during turn-off for high power trench gate/field-stop IGBT modules," in *Proc. IEEE Appl. Power Electron. Conf.*, 2016, pp. 499–504.
[7] J. Chen, E. Deng, L. Xie, X. Ying, and Y. Huang, "Investigations on averaging mechanisms of virtual junction temperature determined by VCE(T) method for IGBTs," *IEEE Trans. Electron Devices*, vol. 67, no. 3, pp. 1106–1112, Mar. 2020.
[8] R. Gelagaev, P. Jacqmaer, and J. Driesen, "A fast voltage clamp circuit for the accurate measurement of the dynamic on-resistance of power transistors," *IEEE Trans. Ind. Electron.*, vol. 62, no. 2, pp. 1241–1250, Feb. 2015.
[9] G. Zeng, H. Cao, W. Chen, and J. Lutz, "Difference in device temperature determination using p-n-junction forward voltage and gate threshold voltage," *IEEE Trans. Power Electron.*, vol. 34, no. 3, pp. 2781–2793, Mar. 2019.
[10] T. Tang, W. Song, K. Yang, and J. Chen, "A junction temperature online monitoring method for IGBTs based on turn-off delay time," *IEEE Trans. Ind. Appl.*, vol. 59, no. 5, pp. 6399–6411, Sep./Oct. 2023.
[11] M. H. M. Sathik, J. Pou, S. Prasanth, V. Muthu, R. Simanjorang, and A. K. Gupta, "Comparison of IGBT junction temperature measurement and estimation methods—A review," in *Proc. Asian Conf. Energy, Power Transp. Electrific.*, Oct. 2017, pp. 1–8.
[12] A. Bryant et al., "Investigation into IGBT dV/dt during turn-off and its temperature dependence," *IEEE Trans. Power Electron.*, vol. 26, no. 10, pp. 3019–3031, Oct. 2011.
[13] Y. Chen, H. Luo, W. Li, X. He, F. Iannuzzo, and F. Blaabjerg, "Analytical and experimental investigation on a dynamic thermo-sensitive electrical parameter with maximum dIC/dt during turn-off for high power trench gate/field-stop IGBT modules," *IEEE Trans. Power Electron.*, vol. 32, no. 8, pp. 6394–6404, Aug. 2017.
[14] Y. Shi, H. Wang, Y. Duan, J. Kang, and Z. Xin, "Measurement of maximum dIC/dt with printed circuit board Rogowski coil for junction temperature estimation of IGBT modules," in *Proc. IEEE Energy Convers. Congr. Expo.*, 2022, pp. 1–6.
[15] D. Garrido, I. Baraia-Etxaburu, J. Arza, and M. Barrenetxea, "Simple and affordable method for fast transient measurements of SiC devices," *IEEE Trans. Power Electron.*, vol. 35, no. 3, pp. 2933–2942, Mar. 2020.
[16] D. Huang, G. Tan, C. Geng, J. Zhang, and C. Liu, "Extraction of junction temperature of SiC MOSFET module based on turn-on dIds/dt," *Engrgies*, vol. 11, no. 8, pp. 1–15, 2018.
[17] M. Baessler, P. Kanschat, F. Umbach, and C. Schaeffer, "1200 V IGBT4high power- A new technology generation with optimized characteristic for high current modules," in *Proc. Int. Exhib. Conf. Power Electron., Intell. Motion Power Qual.*, 2006, pp. 27–30.
[18] J. Schumann and H. G. Eckel, "Charge carrier extraction IGBT model for circuit simulators," in *Proc. Int. Conf. Power Electron. Motion Control*, 2012, pp. 1–7.
[19] B. J. Baliga, *Fundamentals of Power Semiconductor Devices*. Berlin, Germany: Springer, 2008.
[20] W. Feiler, W. Gerlach, and U. Wiese, "On the turn-off behavior of the NPT-IGBT under clamped inductive loads," *Solid-State Electron.*, vol. 39, no. 1, pp. 59–67, 1996.
[21] V. K. Khanna, *Insulated Gate Bipolar Transistor IGBT Theory and Design*. Hoboken, NJ, USA: Wiley, 2003.
[22] Y. Yang and P. Zhang, "In situ insulated gate bipolar transistor junction temperature estimation method via a bond wire degradation independent parameter turn-OFF V_{ce} overshoot," *IEEE Trans. Ind. Electron.*, vol. 68, no. 10, pp. 10118–10129, Oct. 2021.
[23] Y. Shi, Z. Xin, P. C. Loh, and F. Blaabjerg, "A review of traditional helical to recent miniaturized printed circuit board Rogowski coils for power-electronic applications," *IEEE Trans. Power Electron.*, vol. 35, no. 11, pp. 12207–12222, Nov. 2020.
[24] J. N. Fritz, C. Neeb, and R. W. De Doncker, "A PCB integrated differential Rogowski coil for non-intrusive current measurement featuring high bandwidth and dv/dt immunity," in *Proc. Power Energy Student Summit*, 2015, Paper S05.2.
[25] *Standard IPC-2221A: Generic Standard on Printed Board Design*, IPC, 2003. [Online]. Available: https://www-eng.lbl.gov/~shuman/NEXT/CURRENT_DESIGN/TP/MATERIALS/IPC-2221A(L).pdf
[26] High Accuracy AC Current Measurement Reference Design Using PCB Rogowski Coil Sensor, TI, Texas, USA, Jun., 2017. [Online]. Available: https://www.ti.com.cn/cn/lit/ug/tidubv4a/tidubv4a.pdf
[27] W. F. Ray and C. R. Hewson, "High performance Rogowski current transducers," in *Proc. Conf. Rec. 2000 IEEE Ind. Appl. Conf., 35th IAS Annu. Meeting World Conf. Ind. Appl. Elect. Energy*, 2000, vol. 5, pp. 3083–3090.
[28] OPA615, Wide-Bandwidth DC Restoration Circuit, Tektronix Inc., 2009. [Online]. Available: https://www.ti.com.cn/
[29] Versatile Sample & Hold Circuit for Industrial and T&M Applications, Tektronix Inc., 2013. [Online]. Available: https://www.ti.com/lit/ug/tidu155a/tidu155a.pdf
[30] Measure small impedances with Rogowski current probes, EDN, 2014. [Online]. Available: https://www.edn.com/measure-small-impedances-with-rogowski-current-probes/
[31] ABCs of Probes, Tektronix Inc., 2013. [Online]. Available: https://www.tek.com/document/primer/abcs-probes-primer
[32] FF75R12RT4, Insulated Gate Bipolar Transistor, Infineon, 2013. [Online]. Available: https://www.infineon.com

Yafei Shi was born in Hebei, China, in 1996. He received the B.S. degree in electrical engineering from the Harbin University of Science and Technology, Harbin, China, in 2018. He is currently working toward the Ph.D. degree in electrical engineering with Hebei University of Technology, Tianjin, China.

In 2022, he was a visiting Ph.D. student with the Department of Energy Technology, Aalborg University, Aalborg, Denmark. His research interests include Rogowski current sensor and condition monitoring of power electronic systems.

Boyang Zhang was born in Hebei, China, in 2000. He received the B.S. degree in electrical engineering in 2022 from the Hebei University of Technology, Tianjin, China, where he is currently working toward the Ph.D. degree in electrical engineering.

His research interests include wide band-gap semiconductor sensing and device integration.

Jianlong Kang (Student Member, IEEE) was born in Hebei, China, in 1995. He received the B.S. degree in safety engineering from the Xi'an Shiyou University, Xi'an, China, in 2018. He is currently working toward the Ph.D. degree in electrical engineering with the Hebei University of Technology, Tianjin, China.

In 2021, he has been a visiting Ph.D. student with the College of Electrical Engineering, Zhejiang University, Hangzhou, China. His research interests include SiC MOSFETs failure mechanism and degradation monitoring.

Yaokang Lai was born in Zhejiang, China, in 1984. He received the B.S. degree in detection guidance and control technology from the Beijing University of Aeronautics and Astronautics, Beijing, China, in 2007, and the M.S. degree in electronic and communication engineering from the Tsinghua University, Beijing, China, in 2017. He is currently working toward the Ph.D. degree in electrical engineering with the Harbin Institute of Technology, Harbin, China.

Since 2022, he has been as the Chief Engineer with the Beijing Ketong Electronic Relay General Factory Company, Ltd., Beijing, China. His research interests include reliability of solid state relays and solid state power controllers.

Huai Wang (Senior Member, IEEE) received the B.E. degree in electrical engineering from the Huazhong University of Science and Technology, Wuhan, China, in 2007 and, the Ph.D. degree in power electronics from the City University of Hongkong, Hong Kong, in 2012.

He was a Visiting Scientist with the ETH Zurich, Switzerland, form August to September 2014, and with the Massachusetts Institute of Technology, MA, USA, from September to November 2013. He was with the ABB Corporate Research Center, Switzerland, in 2009. He is currently a Professor with the Center of Reliable Power Electronics, Department of Energy Technology, Aalborg University, Aalborg, Denmark. His research interests include the fundamental challenges in modeling and validation of power electronic component failure mechanisms, and application issues in system-level predictability, condition monitoring, circuit architecture, and robustness design.

Dr. Wang is the recipient of Richard M. Bass Outstanding Young Power Electronics Engineer Award from the IEEE Power Electronics Society in 2016 and the 1st Prize Paper Award from IEEE TRANSACTIONS ON POWER ELECTRONICS in 2021. He serves as an Associate Editor of *Journal of Emerging and Selected Topics in Power Electronics* and IEEE TRANSACTIONS ON POWER ELECTRONICS. He was elected as a Member of the Danish Academy of Technical Sciences in 2023.

Zhen Xin (Member, IEEE) received the B.S. and M.S. degrees in electrical engineering from the College of Information and Control Engineering, China University of Petroleum, Qingdao, China, in 2011 and 2014, respectively, and the Ph.D. degree in electrical engineering from Aalborg University, Aalborg, Denmark, in 2017.

In 2016, he was a Visiting Scholar with the University of Padova, Padova, Italy. From 2017 to 2018, he was a Postdoctoral Research Fellow with the Chinese University of Hong Kong, Hong Kong. Since 2018, he has been with the Hebei University of Technology, Tianjin, China, as a Professor. His research interests include condition monitoring of WBG-based power-electronic systems, modeling and validation of power electronic component failure mechanisms, and modeling and control of power converters for renewable energy systems.